Journal of The
Electrochemical Society

Two-Phase Fluid Dynamics in Proton Exchange Membrane Fuel Cells: Counter-Flow Liquid Inlets and Gas Outlets at the Electrolyte-Cathode Interface

To cite this article: Danan Yang *et al* 2024 *J. Electrochem. Soc.* **171** 104501

Journal of The Electrochemical Society, 2024 **171** 104501

Two-Phase Fluid Dynamics in Proton Exchange Membrane Fuel Cells: Counter-Flow Liquid Inlets and Gas Outlets at the Electrolyte-Cathode Interface

Danan Yang,[1,z] Steven B. Beale,[2,3] Himani Garg,[1] and Martin Andersson[1]

[1]*Department of Energy Sciences, Faculty of Engineering, Lund University, SE-221 00 Lund, Sweden*
[2]*Forschungszentrum Jülich GmbH, Institute of Energy Technologies, 52425 Jülich, Germany*
[3]*Mechanical and Materials Engineering, Queen's University, Kingston ON K7L 3N6, Canada*

Understanding the counter-flow of liquid inlet and gas outlet at the interface between the electrolyte and cathode gas diffusion layer (GDL) is crucial for water management in proton exchange membrane fuel cells. Existing studies typically overlook air outlets and assume a fixed liquid inlet direction. This study uses a volume of fluid method to model two-phase interactions in a T-shaped GDL and gas channel (GC) assembly, with GDL geometry derived from nano-computer tomography. Considering potential electrode deformations, such as local cracks and blockages, this research investigates the impact of the size and shape of liquid invasion on the liquid-gas behavior in the cathode GDL and GC using five liquid injection configurations. Simulations also incorporate GDL gas outlets, integrating them with a tailored liquid inlet setup. Results show that the injection site and configuration significantly affect water behavior in the GDL, affecting saturation, stabilization, and breakthrough, followed by drainage in the GCs. Comparisons of simulations with and without air outflow show distinct counter-flow interactions, highlighting variations in water distribution and discrepancies in two-phase transport across the GCs.
 [DOI: 10.1149/1945-7111/ad7d3d]

Manuscript submitted June 6, 2024; revised manuscript received September 11, 2024. Published October 3, 2024.

Supplementary material for this article is available online

Proton exchange membrane fuel cells (PEMFCs) are attractive electrochemical devices for energy conversion in vehicles and stationary power applications, due to their relatively high efficiency, fast response, and low environmental impact compared with conventional power sources. Gas diffusion layers (GDLs) are employed in PEMFCs for gaseous reactant transport and liquid water removal, electrical and thermal conduction, as well as mechanical support for side components. The most typical GDL is a fibrous porous medium made of carbon fiber, whose complex internal structure and possible hydrophobic coating treatment can lead to competition between the transport paths of liquid water products and gaseous reactants. In detail, unreasonable water behavior inside this component, such as flooding or dehydration, will impact reactant transport, electrochemical reaction rate, and ultimately global fuel cell performance. An in-depth understanding of the two-phase flow in a GDL and its associated components is critical to optimizing global high-efficiency, stable, and durable performance and accelerating commercialization.

Two-phase flow behavior in GDLs has been studied experimentally and numerically in recent years.[1–3] In-situ experiments allow the water motion in operating PEM fuel cells to be observed using high-resolution scanning techniques such as synchrotron X-ray radiography.[4,5] Due to the high cost of instrumentation and non-removable occlusion restrictions for inspection and measurement, both ex-situ experiments[6,7] and two-phase simulations[8] have been employed to observe and characterize the inside detailed water behavior as well. In these studies, direct liquid injection from small pores is widely utilized to simulate liquid production from electrochemical reactions. A representative ex-situ experiment setup for GDL two-phase flow can be found in the work of Mularczyk et al.[7] It includes a GDL that is sandwiched between a flow field plate and a water injector. Water is input into the central part of the bottom surface of the adopted GDL. To prevent the water from spreading uncontrollably between the injector field and the GDL, a hydrophobic gasket with a circular hole is placed between the injector and the GDL. Based on this setup, percolating water cluster dynamics are observed by combining X-ray radiography and X-ray tomographic microscopy during consecutive droplet formation cycles on the GDL surface. Lu et al.[9] have utilized a similar setup and studied the liquid breakthrough and intermittent drainage characteristics from GDLs with and without microporous layers (MPLs); The liquid water is input from three small holes connecting the GDL/MPL bottom and a water chamber. It was found that MPL incorporation could stabilize the breakthrough location and limit the number of water injections into a GDL, thus decreasing the liquid content within the GDL.

Liquid inlets have been designed differently in numerical studies on GDL two-phase flow. Multi-phase flow in porous media has been simulated using Eulerian-Eulerian[10,11] models, Eulerian-Lagrangian[12] models, and so-called mixture models.[13,14] Although these approaches can distinguish two or more phases, the phase boundaries become smeared, in practice, due to volume-averaging and numerical diffusion. Each computational cell has a volume fraction for phase i, α_i, such that $0 \leqslant \alpha_i \leqslant 1$ without any precise knowledge of the local distribution of phase i within the cell. Conversely, a series of interface-resolved methods for two (or more) immiscible phases, including the volume of fluid (VOF),[15] lattice Boltzmann,[16] level-set,[17] and phase-field[18] methods, have received more attention when considering liquid water behavior. In these methods, the liquid inlets can be specified in specific regions using scalar boundary conditions, e.g., the phase volume fraction $\alpha_l = 1$ means liquid in VOF. To better discuss the simulations involving these methods, they are divided into two scenarios: with or without employing MPL. For the category without MPL, the liquid water inlet is designed for the GDL bottom with small openings (single or multiple)[18–22] or the entire bottom.[23–31] Niblett et al.[20] have performed dynamic two-phase flow simulations using the VOF method (in OpenFOAM) to evaluate the water distribution in ordered and disordered porous media and obtained comparable results against micro-computed tomography image datasets. Niu et al.[23] have conducted isothermal and incompressible VOF simulations and their results are comparable with experimental X-ray data on GDL through-plane water distribution. Besides, Sun et al.[18] have adopted a phase-field model with the Cahn-Hilliard and Navier-Stokes equations to investigate the effects of contact angle, porosity, and temperature on GDL water breakthrough. In a prior study,[29] the effect of GDL fiber diameter has been considered by combining stochastic GDL reconstructions and two-phase flow simulations. The results show that a larger fiber diameter, around 20 μm, is advantageous in generating larger pores while maintaining a constant porosity, leading to enhanced water removal and reduced water accumulation within the GDL, compared

[z]E-mail: danan.yang@energy.lth.se

with the general fiber diameter range of 6–10 μm. However, the influence of varying fiber diameters on thermal and electronic conductivity is not clear.

It has been experimentally observed by Weber et al.[32,33] that MPL cracks provide specific entry points into GDLs for liquid water. Numerous studies have investigated two-phase flow within GDLs connected to MPLs.[34–39] However, MPL structural configuration varies with the adopted simulation methods. In lattice Boltzmann simulations, the MPL structure is typically represented by a slightly dense lattice with small porosity. One of the outstanding features of the lattice Boltzmann method is that it can handle mesoscale simulations, which enables us to observe the liquid flow in small pores. In such scenarios, the GDL liquid inflow is regulated by the outflow from the MPL. Correspondingly, the liquid inlet treatment is also different in various studies. Kim et al.[34] and Ira et al.[35] utilized the entire MPL bottom surface as the liquid inlet. In addition, Guo et al.[36] designed several small holes on this surface for liquid inlet, with the remaining surface treated as wall boundaries. Nevertheless, there is a common phenomenon in both studies: GDL water inlet location and size are predominantly dictated by the connected MPL structure, such as pore size and water injection conditions in the MPL. Conversely, in two-phase flow methods that solve the Navier-Stokes equations, such as VOF methods, only the cracks present within the MPL are utilized for liquid invasion. This is primarily due to the limitations imposed by the numerical mesh resolution on microscale structures. Additionally, it is observed that water tends to exit the MPL through larger-sized cracks.[38,40] Niblett et al.[37] explored the effects of varying levels of cracks on water and oxygen transport using artificial microporous layer crack dilation. Similarly, Shi et al.[38] analyzed the influence of crack type, distance, and number on GDL water behavior under equivalent crack area conditions, while the latter two factors directly correlate with GDL water saturation. Their findings underscore the impact of differing crack areas on GDL water saturation levels due to capillary fingering, resulting in non-uniform water infiltration through MPLs. Furthermore, Yu et al.[41] investigated the effects of crack area, aspect ratio, width, and depth in GDLs on water behavior during the initial invasion phase. From all the above MPL-included studies, some general remarks are: (1) Cracks benefit the liquid invasion; (2) Liquid breaks through the MPL from random positions, and there is a sudden increase in through-plane liquid water saturation in the MPL/GDL transition region, indicating a spreading behavior; (3) Liquid spreading in the transition region varies in different locations. Besides, Zhang et al.[40] also found that vertical cracks in the catalyst layer toward the cathode also lead to increased water saturation in the vicinity.

Although numerous GDL structure parameters have been considered in both simulations and ex-situ experiments to investigate their influence on liquid water behavior, e.g., wettability,[35] porosity,[36] compression,[42] and thickness,[43] to the best of the authors' knowledge, there is no standardized approach to determining the liquid inlet parameters in these studies, such as liquid inlet location, number, and size. Hence, the effect of these parameters is rarely discussed. Random selection of these parameters may result in possible missing information on water transport, which may lead to inappropriate conclusions about experimental or simulation results. Furthermore, in these interface-resolved two-phase flow studies, the liquid water phase seems to receive more attention than the gas phase. Some studies do not even discuss the gas phase,[28,29,44] resulting in a limited comprehension of the liquid-gas interaction dynamics within GDLs. To address these knowledge gaps, this work conducts a two-phase flow simulation in a T-shaped GDL and GC domain using the VOF method. The GDL structure is reconstructed from scanning images using nano-computer tomography. A 5×5 chessboard-like block structure at the GDL bottom is used to investigate various liquid injection configurations. In addition, the GDL liquid inlet can be larger than the cracks due to liquid spreading behavior following the MPL breakthrough, which proves the feasibility of the current design. Moreover, to observe the interplay of the liquid and gas counterflow within the GDL, an air outlet boundary condition is applied at four corners of the GDL bottom, facilitating the examination of airflow dynamics from the GC to the GDL and its influence on liquid water behavior. It should be noted that the present study is an extension of previous work.[45]

Model Development

The following assumptions are made for the two-phase flow simulations within the GDLs and GCs:

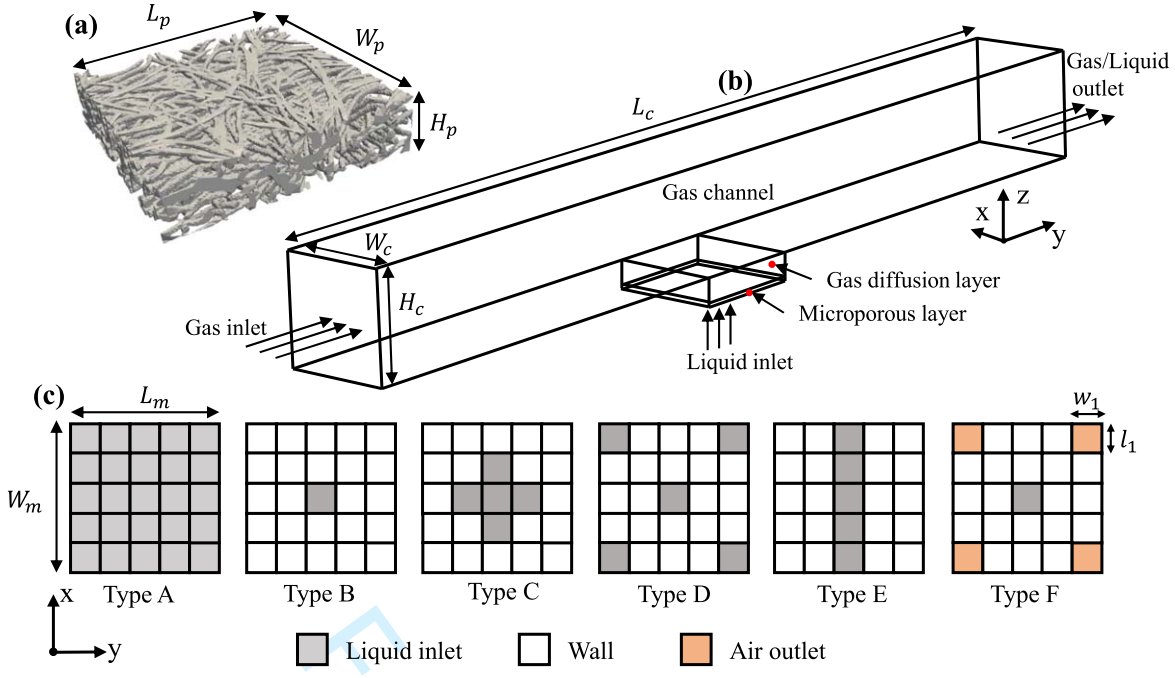

Figure 1. Simulation geometric diagrams. (a) Reconstructed gas diffusion layer sample Freudenberg H2315. (b) The simulation domain contains the GDL, GC, and a thin microporous layer. (c) Liquid water injection types considering different inlet sizes and shapes (Type A, B, C, D, E, and F).

Table I. Dimensional parameters of the reconstructed "T-shape" geometry.

Parameters	Symbol	Value	Unit
Channel length	L_c	4500	μm
Channel width	W_c	500	μm
Channel height	H_c	500	μm
GDL length	L_p	500	μm
GDL width	W_p	500	μm
GDL thickness	H_p	117	μm
Thin layer length	L_m	500	μm
Thin layer width	W_m	500	μm
Thin layer thickness	H_m	10	μm
Thin layer unit cell length	l_1	100	μm
Thin layer unit cell width	w_1	100	μm

Table II. Phase properties at a temperature of 60 °C.

Parameter	Symbol	Value	Unit
Water (Liquid) density	ρ_l	983	kg/m^3
Air (Gas) density	ρ_g	1.06	kg/m^3
Water dynamic viscosity	μ_l	466×10^{-6}	Pa·s
Air dynamic viscosity	μ_g	20×10^{-6}	Pa·s
Surface tension	σ	0.0644	N/m

1. Unsteady, laminar, incompressible, and immiscible flow of gas (air) and liquid (water).
2. Isothermal fluid domain with negligible condensation and evaporation effects for 18 ms two-phase flow simulations.[15,20,23]
3. Constant fluid transport and solid surface properties.
4. Accelerated liquid injection mass flow rate.

Simulation geometry.—Geometric diagrams for simulations are shown in Fig. 1. A Freudenberg H2315 GDL sample reconstructed by experimental scanned image sequence in Fig. 1(a) is utilized to emulate the natural water and gas flow transport within fibrous GDL, instead of employing a homogeneous porous domain represented by a given porosity. A long GC and a thin layer are designed on two sides of the GDL, forming a T-shaped simulation domain in Fig. 1(b). The extended length of the GC ensures fully developed gas flow in the former region and facilitates observation of water movement in the latter. The thin layer of 10 μm under the GDL is employed to design different water injection configurations, as shown in Fig. 1(c). This thin layer can be seen as a simplified MPL. As discussed in the Introduction section, both full and partial liquid inlet boundary conditions have been adopted in previous studies.[20,24] Here, Type A is a full liquid injection. Type B - F are different partial liquid injections accounting for area, location, and air outflow conditions. Table I lists the key structural parameters. Only the liquid region has a thickness of 10 μm, while the other regions (walls or air outflow boundaries) have a thickness of 0 μm, which is the actual GDL bottom surface. Similar strategies for elongating the water injection port can be found in previous works.[15,20,23]

Volume of fluid method.—In the present work, the two-phase flow simulations are conducted using the *interFoam* solver in the open-source software OpenFOAM (version 7). The algebraic VOF approach used here belongs to the family of interface-capturing methods. For this water-gas system featuring high density and viscosity contrast, the interfacial flow is governed by the two-phase Navier-Stokes equations in the single-field formulation. This can be derived through a conditional volume-averaging technique from the local Navier-Stokes equations,[46] considering jump and transmission conditions for mass and momentum at the fluid interface. The closed form reads, for incompressible flow:

$$\nabla \cdot (\mathbf{U}) = 0 \quad [1]$$

$$\frac{\partial(\rho \mathbf{U})}{\partial t} + \nabla \cdot (\rho \mathbf{U}\mathbf{U}) = -\nabla p + \rho \mathbf{g} + \nabla \cdot (\mu \nabla \mathbf{U}) + \mathbf{f}_\sigma \quad [2]$$

$$\frac{\partial \alpha}{\partial t} + \nabla \cdot (\alpha \mathbf{U}) = 0 \quad [3]$$

where $\mathbf{U}$ is the liquid-gas mixture velocity vector, and $\mathbf{g}$ is the acceleration due to gravity, acting in the z-direction. The scalar α is integrated across each grid cell within the discretized domain to represent the fluid volume fraction. α_l and α_g represent liquid and gas phases, respectively, and $\alpha_l + \alpha_g = 1$. In each discretized cell, the value of α is unity in the liquid phase and zero in the gas phase, whereas intermediate values are encountered only in cells of the interface region between the two phases. Owing to numerical diffusion, the interface is shown as a region, not an ideal surface, although different methods have been adopted to artificially sharpen the interface.[47]

Here, ρ and μ are the mixture density and dynamic viscosity, defined as phase averages:

$$\rho = \alpha_l \rho_l + \alpha_g \rho_g \quad [4]$$

$$\mu = \alpha_l \mu_l + \alpha_g \mu_g \quad [5]$$

To include capillary force at the fluid interface, the continuous surface force model of Brackbill et al.[48] is employed to close for the volumetric surface tension force $\mathbf{f}_\sigma$, i.e.,

$$\mathbf{f}_\sigma = -\sigma \nabla \cdot \left(\frac{\nabla \alpha}{|\nabla \alpha|} \right) \nabla \alpha \quad [6]$$

Several advection schemes have been described in the literature for the volumetric phase fraction transport equation, Eq. 3. This study employed the multidimensional universal limiter with an explicit solution scheme. This enforces boundedness and sharpness of the volumetric phase fraction field using flux-corrected transport, iteratively.[49–51] Alternatives are to use specialized high-resolution schemes, so-called interface capturing schemes, such as the interface capturing scheme on arbitrary meshes by Ubbink and Issa[52] or the high-resolution interface capturing scheme by Muzaferija and Peric.[53] Notably, there are also geometric VOF methods with support for complex geometries[54] with the potential of capturing the interface evolution at high accuracy. These are considered beyond the scope of the present study.

The coupling between volumetric phase fraction and linear momentum transport, Eqs. 2 and 3, is accomplished in a momentum conservative manner. The mass flux is reconstructed from the discretized transport equation for the advection of the volumetric phase fraction and consistently used after the solution of Eq. 3 with the update of mixture quantities in the convection term of the discretized linear momentum equation.

The time step is chosen to fulfill the Courant-Friedrichs-Lewy condition based on the fluid, interface, and capillary velocity. The latter is employed to reduce spurious velocities and is defined as[55]

$$Co_{cap} = \sqrt{\frac{2\pi\sigma}{(\rho_g + \rho_l)V}} \Delta t \quad [7]$$

with V denoting the mean cell volume and Δt the time step. Fluid properties are listed in Table II.

Table III. Air and water inlet velocity values for different GDL water inlet types and contact angles of key surfaces.

Parameter	Value	Unit
Air inlet velocity	(0 10 0)	m/s
Water inlet velocity		
Type A	(0 0 0.02)	m/s
Type B	(0 0 0.5)	m/s
Type C	(0 0 0.1)	m/s
Type D	(0 0 0.1)	m/s
Type E	(0 0 0.1)	m/s
Type F	(0 0 0.5)	m/s
Contact angle		
GC top and two side surfaces	45	°
GDL/GC interface	150	°
GDL four side surfaces	150	°
GDL surface	150	°

Boundary and initial conditions.—For the velocity field, the GC and MPL inlets are set with uniform gas and water velocity boundaries, $\mathbf{U}_g$ and $\mathbf{U}_l$, respectively. Considering the small computational domain of the GDL and the relatively short run-time, all subsequent simulated cases use the same constant water inlet mass flow rate, to eliminate the effect of the liquid injection flow rate $\dot{m}$. This approach has been popularly adopted in previous studies.[20,23]

The water inlet velocity for each type of water injection pattern is calculated by Eq. 8, and specific values are summarized in Table III. ρ and A are the fluid density and cross-sectional area, respectively.

$$\mathbf{U}_{l,in} = \frac{\dot{m}}{\rho A} \quad [8]$$

A zero gradient velocity $\nabla\mathbf{U}\cdot\hat{\mathbf{n}} = 0$ is enforced at the GC outlet ($\hat{\mathbf{n}}$ is a unit normal vector), with all other walls set with zero velocity $\mathbf{U} = \mathbf{0}$ m/s. Total pressure $p = 0$ is set for the GC outlet and *fixedFluxPressure* boundary condition (Documented in the C++ Source Code Guide of OpenFOAM v7) for the remaining surfaces. Here, p equals $p_s + 1/2\rho U^2$, where p_s is the static pressure and U is the velocity magnitude. In the water fraction field, phase volume fraction $\alpha_g = 0$ and $\alpha_l = 1$ are assigned to represent gas and liquid inlets, respectively. Surface wettability is considered through the utilization of static contact angles. Hydrophilic boundary conditions are imposed on the GC top and two side surfaces, whereas the GDL surface, all MPL surfaces, and the GDL/MPL interface are made hydrophobic. Specific contact angle values are shown in Table III. Symmetry boundary conditions are enforced on the four sides of the GDL. The above boundary conditions apply to all cases (from type A to type F). However, for Type F, the air outlet at the four corners of the GDL/MPL interface is configured with $\nabla\mathbf{U}\cdot\hat{\mathbf{n}} = 0$, $\nabla\alpha_l = 0$, and $p = 0$. The aim is to examine the interaction between air and water counter-flow and incorporate a more realistic boundary condition in future investigations.

To speed up simulations and save computational cost, in previous numerical studies, liquid behavior in GDLs and GCs is simulated by adopting an accelerated velocity.[15,20,23] The adopted liquid input velocity is found to vary in the range of 0.014-1 m/s.[20,23,29,44] An experimental water injection velocity of 2.97×10^{-5} m/s in Niblett et al.[20] has been increased approximately a thousand times in the corresponding simulations, and reasonable simulation results against experiments are obtained. Similar verifications can be found in Ref. 15, 23. In addition, the blocks under the GDL in this study are designed based on (a) the random and discrete water breakthrough that occurs at the interface between the microporous layer and GDL, attributed to capillary fingering flow;[56,57] (b) MPL cracks of diverse sizes and shapes,[37,38] as well as (c) GDL perforations.[58]

The mesh for the entire geometry predominantly consists of hexahedral elements generated using the SnappyHexMesh utility in OpenFOAM. A mesh independence study for fibrous GDL was conducted in a previous work[59] and the same mesh strategy has been adopted in the present study. To balance computational cost with simulation accuracy, the grid resolution for each region was set to 8.3 μm × 8.3 μm × 8.3 μm for the GC and 2.08 μm × 2.08 μm × 1.46 μm for the GDL. The mesh resolutions are relatively uniform across each domain, except for the transition between regions. These resolutions are comparable to those used in previous numerical two-phase studies, which range from 13 μm[20] to 25 μm[60] for GCs and 1.5 μm[26] to 6.8 μm[20] for GDLs, respectively.

Calculations.—To quantitatively compare the different liquid injection types, slice water saturation, total water saturation, capillary pressure, and pressure drop are discussed using the following calculations. Considering the interface diffusion in volume of fluid simulations, as for liquid saturation, an isosurface of $\alpha_l = 0.5$ has been widely adopted to distinguish between the two phases,[17,37,61] namely the region with $\alpha_l \geqslant 0.5$ is regarded as liquid phase. This value was also selected for interface reconstruction in VOF method development.[62] The interface location is thought to be independent of the grid size because of the small grid resolution in this work. Furthermore, the interface thickness should be uniform in the grid cell of GDL and GC because of the relatively constant grid resolution in each domain. The focus of these calculations is exploring the variation trend and mutual dependency of parameters while selecting the isosurface value of α will merely affect the magnitudes.

In-plane GDL slice water saturation, S_s:

$$S_{s,GDL} = \frac{A_l}{A_p} = \frac{\sum_{i=1}^{n_1} A_{l,i}|_{\alpha\geqslant 0.5}}{\sum_{j=1}^{m_1} A_{p,j}} \quad [9]$$

A_l and A_p are the liquid area and pore area in an in-plane slice.

GDL total water saturation, $S_{t,GDL}$:

$$S_{t,GDL} = \frac{V_{l,GDL}}{V_{p,GDL}} = \frac{\sum_{i=1}^{n_2} V_{l,i}|_{\alpha\geqslant 0.5}}{\sum_{j=1}^{m_2} V_{p,j}} \quad [10]$$

$V_{l,GDL}$ and $V_{p,GDL}$ are the liquid volume and pore volume in the entire GDL region.

Capillary pressure, P_c, is the pressure difference across the interface between the two phases, which is a dominant force for GDL capillary fingering water evolution[63,64] because of the small capillary number ($Ca = \mu U/\sigma$). Thus, a critical definition is $P_c = P_l - P_g$, and P_l and P_g are liquid phase pressure and gas phase pressure. Besides, the Young Laplace equation is also widely used to estimate the capillary pressure, defined by $P_c = 2\sigma\cos(\theta)/R$, where R is the effective mean pore radius. As VOF (and other interface-resolved two-phase simulation methods) solves the equations using mixture properties, e.g., μ and ρ, it is still difficult to directly obtain individual liquid and gas pressure from solving results. The calculation of P_c in both existing experiments and VOF simulations is mainly reliant on different post-processing methodologies. To study the relationship between capillary pressure and saturation, Palakurthi et al.[65] and Fairweather et al.[66] regarded the liquid injection pressure as P_c, while the influence of other forces and internal uneven pore structure is ignored. Thus, Mularczyk et al.[64] estimated the interface curvature from scanning images of GDL drainage experiments and calculated P_c based on a modified Young Laplace equation, $P_c = 2\sigma/R$. In addition, the values calculated based on curvature and volume-averaged phase pressure in VOF simulations were compared with those from experiments. It is found that all three P_c have similar magnitude, but P_c based on curvature in VOF simulations can not capture the increasing trend before the

liquid breakthrough. A similar curvature-based strategy has also been employed by Rabbani et al.[67] However, some approximations must be involved in the estimation. To avoid this, Konangi et al.[68] identified two isosurfaces of α, i.e., $\alpha_1 = 0.99$ and $\alpha_2 = 0.01$, in VOF simulations to represent the liquid phase and the gas phase and calculated P_c based on area-averaged pressure difference, and the mathematical expression is,

$$P_c = \Delta P^s = \left.\frac{\sum_{i=1}^{n_3} P_{l,i}A_i}{\sum_{i=1}^{n_3} A_i}\right|_{\alpha=\alpha_1} - \left.\frac{\sum_{j=1}^{m_3} P_{g,j}A_j}{\sum_{j=1}^{m_3} A_j}\right|_{\alpha=\alpha_2} \quad [11]$$

where ΔP^s is the pressure difference, m_3 and n_3 are the number of grid cells that two isosurfaces have occupied. A_i and A_j are the corresponding surface area. In Konangi et al.,[68] the pressure values located in both isosurfaces were mapped into another isosurface with $\alpha = 0.5$, thus m_3 equals n_3, and A_i equals A_j. A similar approach has been employed by Niblett et al.[20] using the area-averaged pressure in isosurface $\alpha = 0.5$. This isosurface is also employed in the current study to calculate P_c. Besides, the P_c values computed from isosurface groups, $\alpha = 0.01$ and 0.99, are also compared. The aforementioned volume-averaged method is expressed below,

$$P_c = \Delta P^v = \left.\frac{\sum_{i=1}^{n_4} P_{l,i}V_i}{\sum_{i=1}^{n_4} V_i}\right|_{\alpha\geqslant 0.5} - \left.\frac{\sum_{j=1}^{m_4} P_{g,j}V_j}{\sum_{j=1}^{m_4} V_j}\right|_{\alpha<0.5} \quad [12]$$

The isosurface of $\alpha = 0.5$ is also employed in the calculation of GC total water saturation, $S_{t,GC}$, and GC pressure drop, $P_{d,GC}$. Specifically, the liquid volume is calculated based on $\alpha \geqslant 0.5$, and $\alpha < 0.5$ is used to extract the gas phase domain and calculate the gas pressure drop.

$$S_{t,GC} = \frac{V_{l,GC}}{V_{b,GC}} = \frac{\sum_{i=1}^{n_5} V_i|_{\alpha\geqslant 0.5}}{\sum_{j=1}^{m_5} V_j} \quad [13]$$

$$P_{d,GC} = P_{in,GC} - P_{out,GC} = \frac{\sum_{i=1}^{n_6} P_{in,i}A_i}{\sum_{i=1}^{n_6} A_i} - \frac{\sum_{i=1}^{m_6} P_{out,j}A_j}{\sum_{j=1}^{m_6} A_j} \quad [14]$$

$V_{l,GC}$ and $V_{b,GC}$ are the liquid volume and bulk volume in the entire GC region. $P_{in,GC}$ and $P_{out,GC}$ are the area-averaged pressure at GC inlet and outlet. This method has been adopted in other VOF simulation studies in PEMFC channels.[69]

Besides, a statistical stabilization state refers to parameters such as saturation and pressure that do not have a long upward or downward trend but reach a certain value or range with little or no fluctuation.[16]

Results and Discussion

VOF methods in OpenFOAM have been widely adopted for the GDL and GC two-phase flow simulations and validated using experimental data.[20,44] Early work by Andersson et al.[15] utilized synchrotron tomography images to validate the droplet detachment and attachment behavior in GCs. In a previous study,[29] the simulated GDL two-phase flow behavior was compared with experimental and numerical results, demonstrating the rationality and reliability of the VOF model setup used. All simulations were executed in parallel on a computer cluster. Each simulation, spanning 18 milliseconds, was computationally intensive, requiring 50880 core hours to complete.

In addition, three representatives of the P_c calculations for Type A are compared, as shown in Fig. A·1 of the Appendix. The analysis reveals that while their magnitudes exhibit noticeable differences, their time-varying trends are similar. When comparing these P_c values with those from previous studies—such as approximately 5800 Pa by Mularczyk et al.,[64] around 3300 Pa by Santamaria et al.,[33] roughly 5700 Pa by Bazylak et al.,[42] 4000-5000 Pa by Niblett et al.,[20] about 6000 Pa by Niu et al.,[31] and 5000-6500 Pa by Santamaria et al.[33]—it is found that the area-averaged P_c in the isosurface of $\alpha = 0.5$ aligns more closely with these previous results. Therefore, this area-averaged value is used for further result discussion.

Effect of different water inlet topology.—This section compares the water behavior within the first five GDLs, corresponding to the liquid intrusion types from Type A to Type E. Figure 2 presents the top view of the 3D water distribution within GDLs across 6 simulation timesteps. In five examined GDLs, especially the Type A GDL, liquid water exhibits features resembling "gorges and ravines", due to the ununiform pore distribution during random fiber stacking during the construction. Experiments have found that capillary fingering water tends to exit the GDL through pathways consisting of large pores.[64] Moreover, according to the Young Laplace equation, a large average pore radius R results in a low capillary pressure P_c to overcome the capillary forces to move a liquid through the pore. Based on this principle, some GDL bottom regions allow liquid water to enter because of the large pores in the in-plane direction. However, it is also observed that parts of the invaded liquid abruptly terminate near the liquid inlet, unable to penetrate further, which is impeded by small through-plane pores. Some advanced approaches have been proposed to improve the GDL drainage by utilizing gradient pore structures along the through-plane direction or perforations.[58] Furthermore, the appearance of water inevitably affects gas transport by changing the effective values of permeability, porosity, diffusivity, and resistance. Zamel et al.[70] have studied the effect of liquid water on GDL transport properties, and hysteresis of relative permeability after liquid imbibition and drainage cycles has also been found.[71] After observing the water evolution over time, it is found that the water removal process within the GDLs is accompanied by spreading, temporary breaks, and stable/unstable connections. However, these features show different levels between different GDLs and even between different regions within each GDL. For instance, liquid in the lower two corners of Type C hardly spreads to further regions, while the GDL with Type B injection includes visible spreading behavior. The difference can be the pore distribution, and also the different liquid velocities. As mentioned by Santamaria et al.,[33] faster injection rates produce numerous smaller breakthrough droplets because of an increasing number of pores available for flow through. Comparative analysis of liquid distribution tomography among the five GDL types indicates that Types A and E reach a quasi-stable state after T = 1.5 ms, whereas the others exhibit minor accumulation until 4 ms, particularly on the left side of the GDLs. Except for the type B GDL, the water distribution within other GDLs hardly changes from 4 to 18 ms, indicating a relatively stable state.

Figure 3(a) demonstrates the temporal evolution of total water saturation across Type A-E GDLs. Notably, substantial differences are evident among five GDLs under identical conditions of liquid injection mass flow rate and GDL geometry, solely attributed to alterations in liquid injection configurations. Each scenario displays rapid water accumulation within the initial 1 ms water injection. Type A GDL, featuring a full liquid inlet, exhibits the most precipitous increase in water saturation. Conversely, Types C-E GDLs, each equipped with five liquid inlet blocks, have an intermediate rate of water accumulation. As the area of liquid injection diminishes, there is a corresponding deceleration in the rate of water accumulation. Subsequent to the liquid breakthrough, the

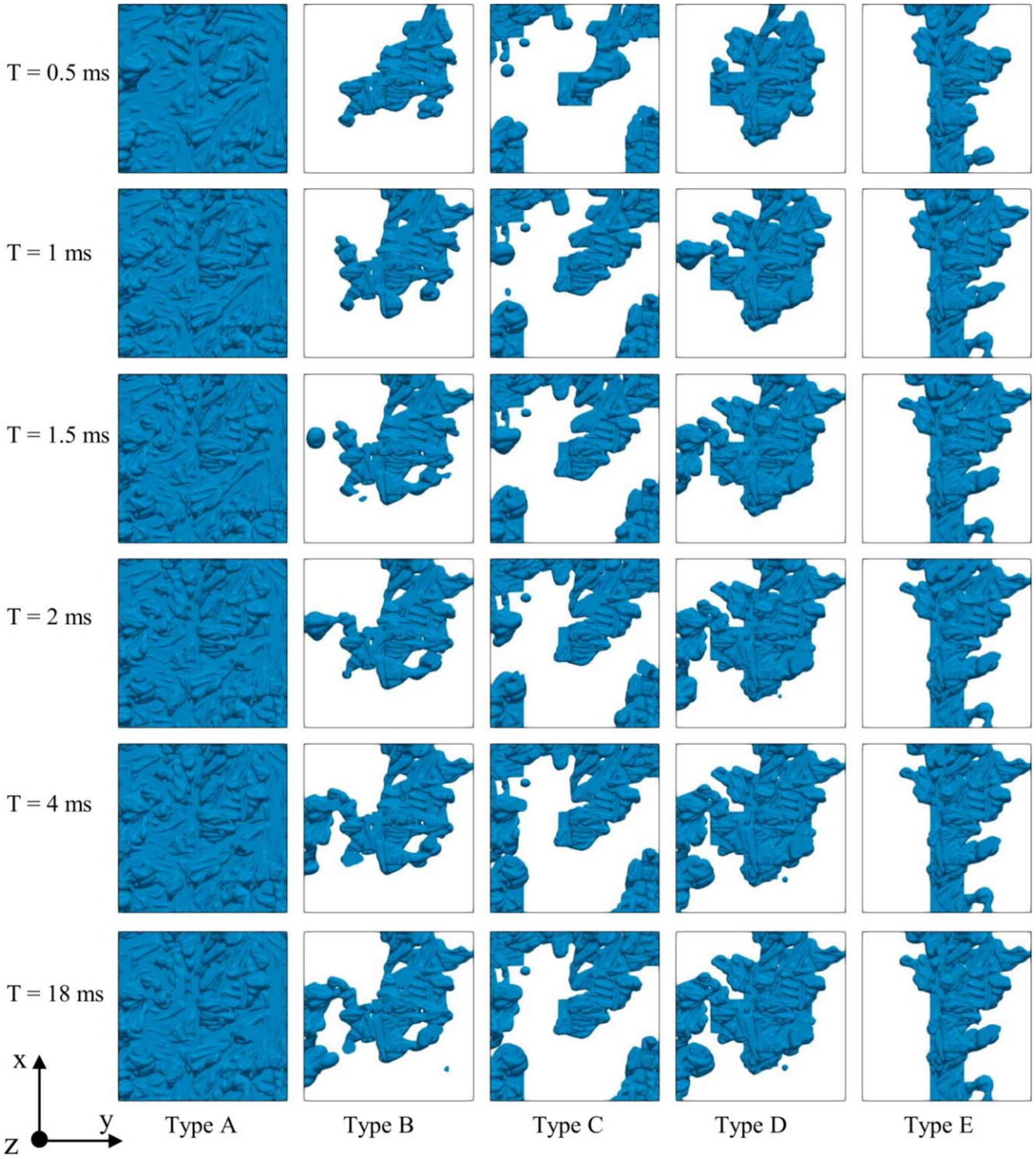

Figure 2. Top view perpendicular to the x-y plane of 3D water flow evolution with different types of liquid inlet configurations at 0.5 ms, 1 ms, 1.5 ms, 2 ms, 4 ms, and 18 ms. Type A: Full liquid inlet; Type B: single central inlet block; Type C: Five inlet blocks with one in the center and four in the corners; Type D: Central cross-shaped five blocks; Type E: Line-shaped five blocks along the x direction.

rate of increase in total water saturation for Types A and E GDLs notably decreases, stabilizing statistically at 0.7 ms and 1 ms, respectively. In contrast, although the other three types (B, C, and D) also show a deceleration in water accumulation post-breakthrough, their saturation levels continue to rise gradually until 6 ms. Among these, Type D GDL, characterized by cross-shaped liquid inlets, exhibits a notably rapid increase, approximating the water saturation levels of Type A GDL by approximately 3 ms. Following this, Type D displays a quasi-periodic fluctuating saturation pattern. This oscillation reflects the water receding phenomenon[20] during breakthrough and subsequent reaccumulation after droplet detachment, as depicted in Fig. 4. This water behavior near the GDL left side results in the fluctuation of total water saturation in other GDL Types. Type B GDL, with a singular central liquid inlet block, maintains the slowest rate of water accumulation, reaching a quasi-periodic fluctuating saturation pattern around 6 ms, lower than the

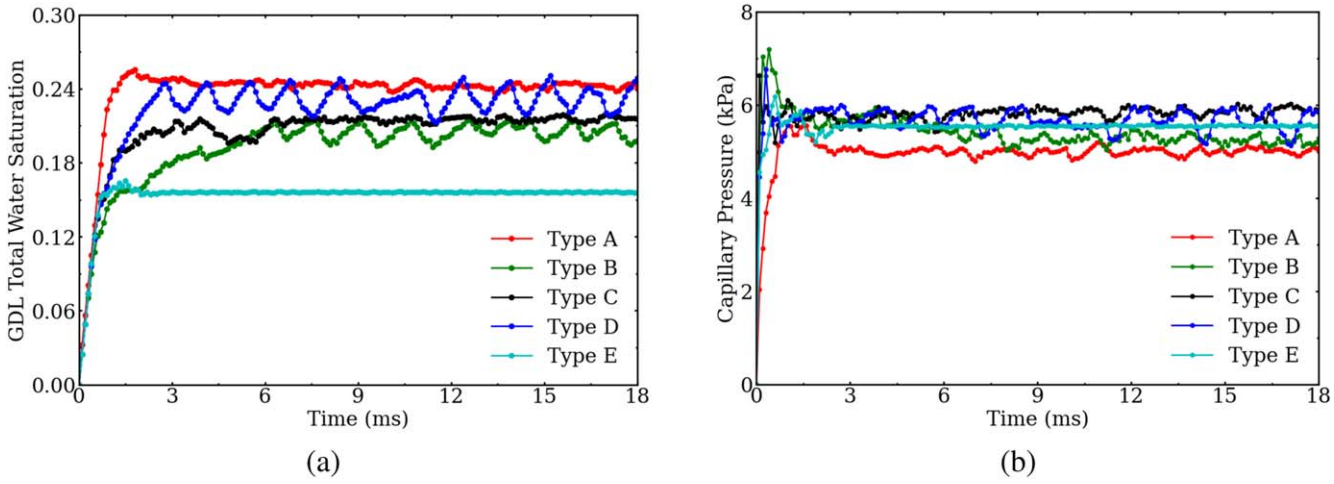

Figure 3. Time-dependent total water saturation and capillary pressure of Type A-E GDLs.

steady saturation of Type C GDL. A commonality observed across all GDL types is that following water breakthrough, the duration required to reach statistical stabilization in total water saturation tends to increase with higher liquid inlet velocities.

Based on the displacement theory in porous media proposed by Lenormand et al.,[72] the two-phase flow pattern in a two-phase system with a high viscosity ratio, approximately 986:1, transitions from capillary fingering flow to stable displacement flow as the liquid inlet velocity increases. A defining characteristic of capillary fingering is that once the non-wetting invading phase penetrates the porous medium, it maintains stability alongside water within the medium. Conversely, in stable displacement flow, the invading phase consistently replaces the defending phase, typically achieving high saturation levels. Therefore, the results highlight the importance of considering flow types within GDLs relative to liquid velocity in practical experiments and simulations. Notably, while Types C, D, and E have identical velocities, consequently the same capillary numbers, their considerable difference in stabilization rates indicates that factors beyond capillary number and viscosity ratio are influential in determining flow dynamics within heterogeneous porous structures. Future research should explore these additional factors to comprehensively understand two-phase flow behaviors.

In Fig. 3(b), the GDL liquid capillary pressure P_c over time is presented. P_c shows a more rapid statistical stabilization compared to GDL total water saturation. Notably, each P_c profile experiences an overshoot coinciding with the initial liquid breakthrough. The magnitude of the overshoot increases with higher liquid injection velocities. Type B-D GDLs take a long time to achieve statistical stabilization. However, they quickly establish a relatively stable capillary pressure, which typically ranges between 5-6 kPa following the breakthrough. Besides, capillary pressure and total water saturation show a similar fluctuation level but exhibit divergence in fluctuation trend during the statistical stabilization process. Type E GDL has a relatively flatter variation in both P_c and water saturation. Type D GDL has the strongest fluctuation in P_c and water saturation, while the fluctuation of P_c is more irregular. A noticeable decline in capillary pressure is observed with a decrease in GDL total water saturation, while a very large increase in GDL total water saturation may correspond to three situations of P_c, e.g., remaining flat, slight increase, and evident increase. Thus, water saturation is more sensitive to the decrease of P_c than an increase. In addition, the capillary pressure in Type A GDL is comparatively lower compared to those scenarios involving partial liquid injections. This discrepancy arises from the equal distribution of liquid afforded by full injection, enabling it to explore larger and shorter pathways, thus reducing the need for elevated capillary pressure. A similar conclusion was obtained by experiments.[64] Conversely, the liquid is compelled to penetrate small-pore regions in other types, resulting in increased capillary pressure. Among all the compared GDLs, the relationship between water saturation and capillary pressure across the types does not exhibit a straightforward inverse correlation. Specifically, Type A GDL demonstrates the highest water saturation yet manifests the lowest capillary pressure. Conversely, Type E GDL, which exhibits the lowest water saturation, presents a moderate capillary pressure. Type C GDL, characterized by a moderate level of water saturation, is associated with the highest capillary pressure among the types evaluated.

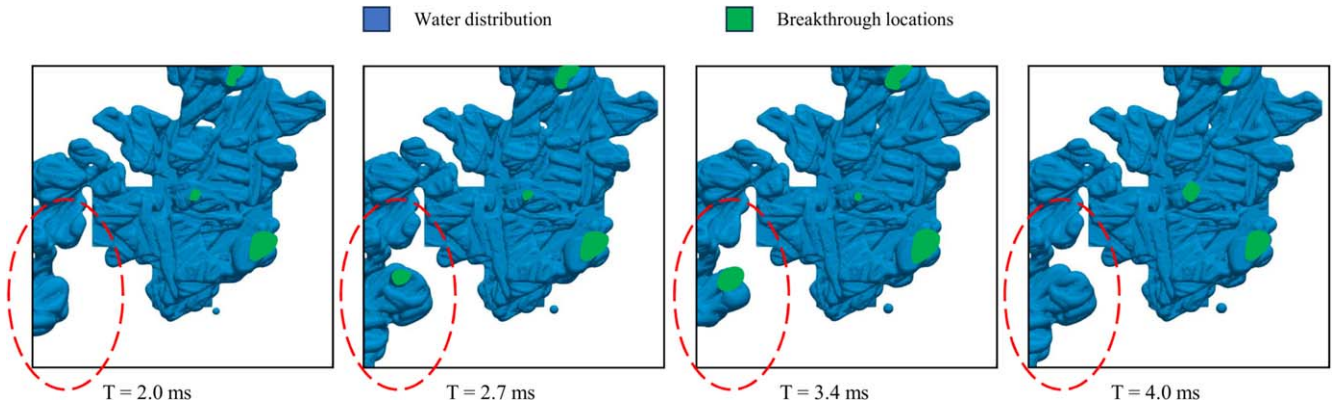

Figure 4. GDL water receding phenomenon during water breakthrough and reaccumulation behavior after droplet detachment in Type D GDL.

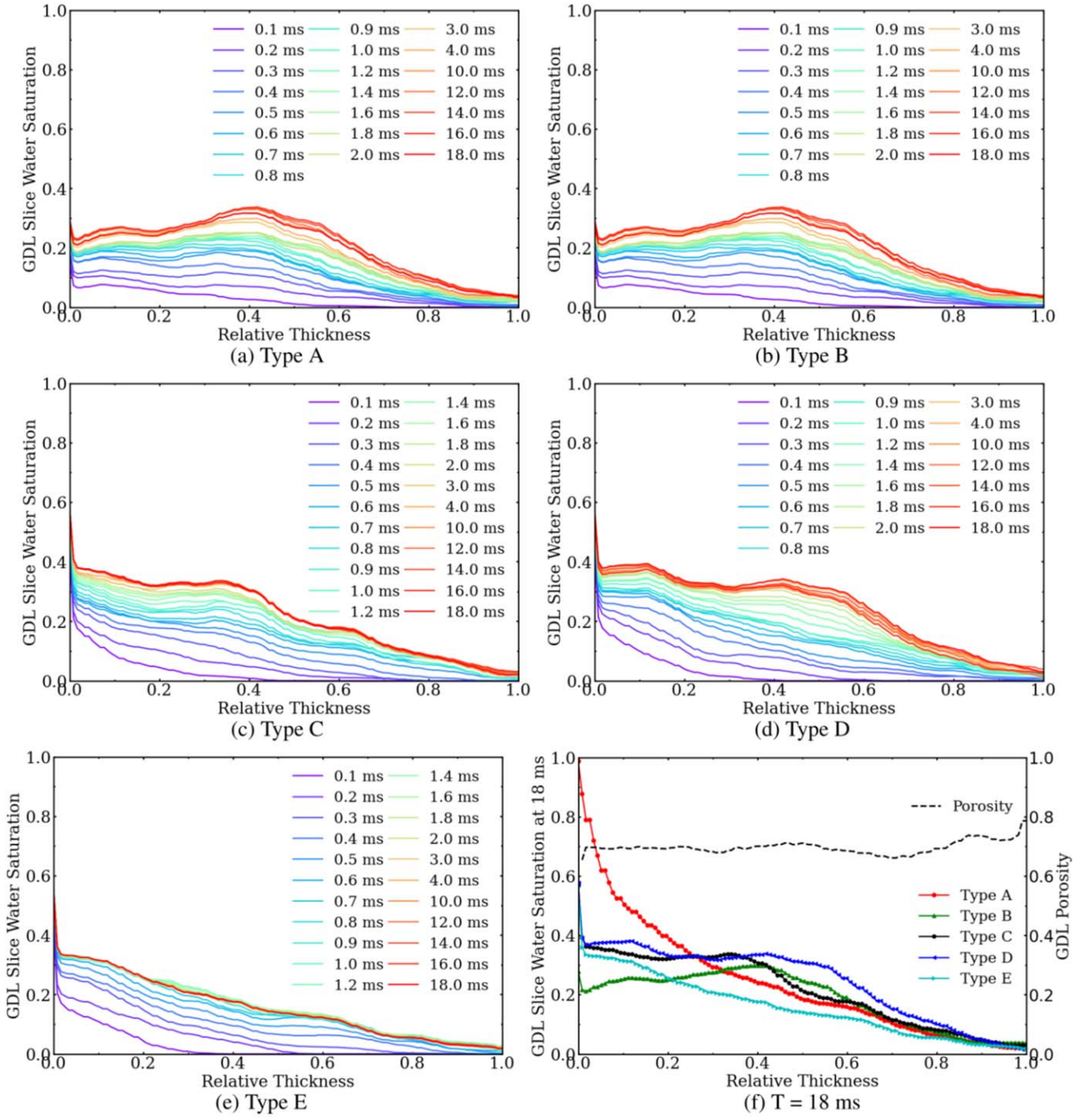

Figure 5. (a)–(e) Through-plane slice water saturation in Type A-E GDLs. (f) Through-plane porosity distribution and slice water saturation at the final simulation time T = 18 ms.

To explore more detailed water dynamics within the GDLs, a detailed analysis of through-plane water distribution as a function of relative thickness is illustrated in Figs. 5a–5e. Each GDL experiences a rapid increase of water along both through-plane and in-plane directions at initial moments. The time-series results demonstrate the statistical stability of water distribution, as evidenced by the gradual proximity of curves at different time-steps, especially from 4 ms to 18 ms. In Type A, a rapid decrease in through-plane saturation near the liquid inlet suggests significant liquid retention at this location. As the liquid spreads, the most dynamic region of water activity shifts toward the central area in the z-direction, spanning a relative thickness from 0.2 to 0.7. Notable saturation contraction is observed in Types A and E GDLs prior to achieving liquid stability, particularly below a relative thickness of 0.4. In contrast, the water content continues to rise in the remaining three types, spreading across distinct regions: predominantly within a relative thickness from 0.1 to 0.4 in Type B; between 0.2 and 0.4 in Type C; and from 0.3 to 0.7 in Type D. Additionally, Types A and E consistently show a decreasing trend in saturation from the GDL/MPL interface (relative thickness 0) to the GDL/GC interface (relative thickness 1), whereas the other three types include varying levels of saturation increase during part of through-plane regions, particularly in Type B.

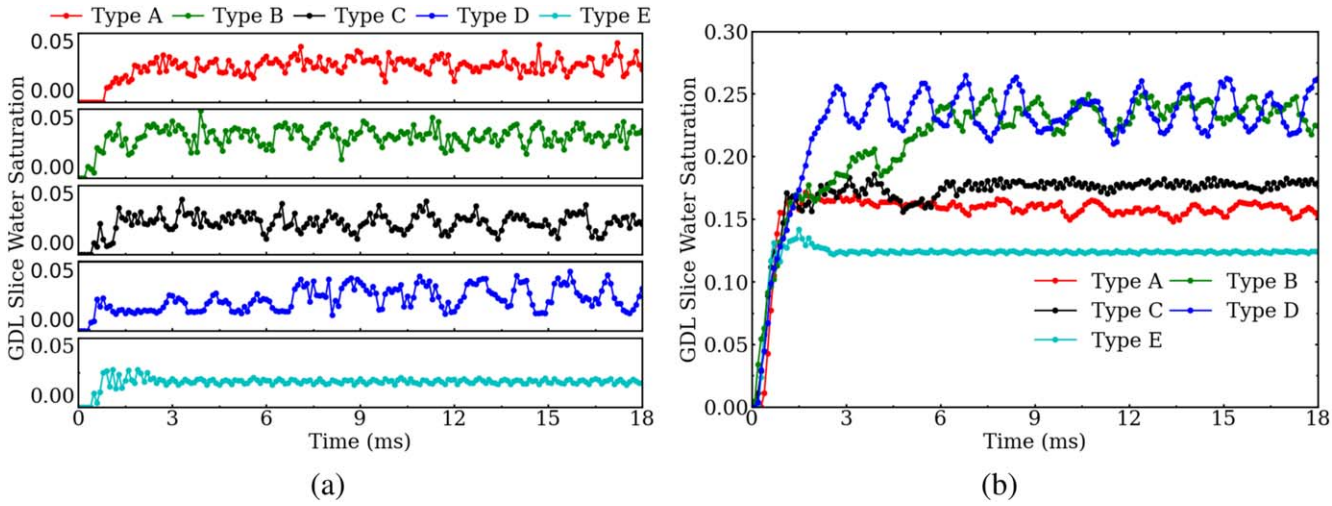

Figure 6. Time-dependent slice water saturation (a) at the GDL/GC interface, (b) at GDL relative thickness of 0.6.

An optimal water management strategy in PEMFCs aims for stable water drainage without excessive occupation of the porous matrix, thereby minimizing gas transport resistance. The water saturation level across different relative thicknesses serves as an indicator of the remaining gas space, and higher slice saturation suggests reduced gas space availability. Figure 5f presents the GDL through-plane porosity distribution and the final saturation state at 18 ms, highlighting that the water space occupation along the thickness direction within the GDL is heavily influenced by the liquid injection area. A more pronounced variation is observed near the liquid injection regions, diminishing progressively toward the GDL/GC interface. Consequently, the liquid injection location and size markedly affect the water saturation in half of the GDL proximate to the liquid inlet. This observation may correspond with findings in prior research[73] that fuel cells with cracked MPLs have enhanced performance under high current density conditions. In such instances, liquid predominantly enters the GDL through cracks, resulting in partial liquid injection. This phenomenon reduces water accumulation near the liquid inlet, thereby increasing the available transport pathways for reactant gases.

The GDL/GC interface is an active place connecting bulk GC and porous GDL, as well as an interacting region of high-speed and slow-speed flow, which inevitably results in droplet instability.[74] Figure 6a illustrates the temporal variation in slice water saturation at the GDL/GC interface for Type A-E GDLs. Although the interface saturation of all GDLs is small, they all exhibit frequent oscillations with large relative deviations. The period when saturation at the interface rises from zero to a nonzero value represents the time GDL water breakthrough occurs. It is found that Type A injection results in the slowest breakthrough between 0.8-0.9 ms, whereas Type B leads to the fastest breakthrough between 0.3-0.4 ms. Types C, D, and E all have breakthroughs between 0.4-0.6 ms. Thus, increasing the liquid inlet velocity may speed up the liquid breakthrough from GDLs. At the GDL/GC interface, Type E GDL has the lowest fluctuation of slice water saturation, followed by Type A. Type B-D GDLs all exhibit strong fluctuation, sometimes exceeding 0.03. Moreover, Fig. 6b shows the time-varying slice water saturation at the relative thickness of 0.6 of all GDLs. Relative thickness is defined as the ratio of the height of an in-plane slice, relative to the GDL bottom, to the GDL whole thickness. Compared with the saturation at the GDL/GC interface, the slice water saturation at this position shows smoother variation with small deviations and bigger saturation. After breakthrough Type A, Type C, and Type E GDLs all quickly reach saturation stabilization with small oscillations, while slice water saturation of Type B and Type D GDLs all show bigger quasi-periodic oscillations around 0.24 after a certain time. The result implies that with partial liquid injection employed, water may occur slow breakthrough and accumulate within the central region of these three GDLs.

The water saturation oscillation at the GDL/GC interface can reflect the detachment and attachment behavior of water; that is, the more frequent the oscillation, the more water droplets detach near the center area of the GDL/GC interface, and the oscillation amplitude positively reflects the liquid droplet size. On the contrary, relatively smooth changes indicate more water adhesion on the GC sidewalls or detachment of droplets away from the central region of the interface. Figure 7 shows the water distribution within the GCs at four moments: 2 ms, 3 ms, 4 ms, and 18 ms. All scenarios have water attachments on at least one GC side wall. Firstly, liquid injection types can affect the breakthrough location in the GDL/GC interface. Compared to the situation of connecting to Type A GDL, it can be found that the breakthrough location is approximately on the top side of the GDL bottom liquid injection once partial liquid injections are adopted. For example, a main breakthrough in the GDL/GC interface center in Type B (with a single central inlet) and four liquid breakthrough locations near the four GDL corners in Type C (with one single central inlet and four corner inlets). Then, different breakthrough features bring significant water behavior within the GCs.

Specifically, Type A and Type E injections have water attached to both side walls, which might be the reason why they become statistically stabilized early. Unlike the droplet detaching upon the GDL/GC interface, the water attachment on hydrophilic side walls and further top wall can create a relatively stable liquid flow pattern.[75,76] As a result, the water within the GDL might not have to find other paths to break through. However, for the other three scenarios with Type B-D, the fluctuation during droplet growth and detachment may transfer to water within GDL and lead to new water advancing or receding phenomenon. For instance, Niblett et al. found that GDL receding water accumulation is caused by the growth of GC droplets and later detachment[20] in their 2D and 3D two-phase simulations. Additionally, Type B experiences significant droplet detachment near the interface, leading to large fluctuations in water saturation, as shown in Fig. 6a. In contrast, Type D demonstrates a more stable and lower variation in water saturation due to two factors: attachment on the side wall and detachment occurring farther from the interface, with less water detachment occurring near the interface.

Figure 8a displays the time-varying GC water saturation under different GDL liquid injection types. The modes of water attachment and detachment affect water accumulation within the GC. Approximately 14 ms after injection, the GCs connected to Type B-D GDLs exhibit statistically stable water saturation levels, whereas the GC connected to Type A GDL shows a rising trend

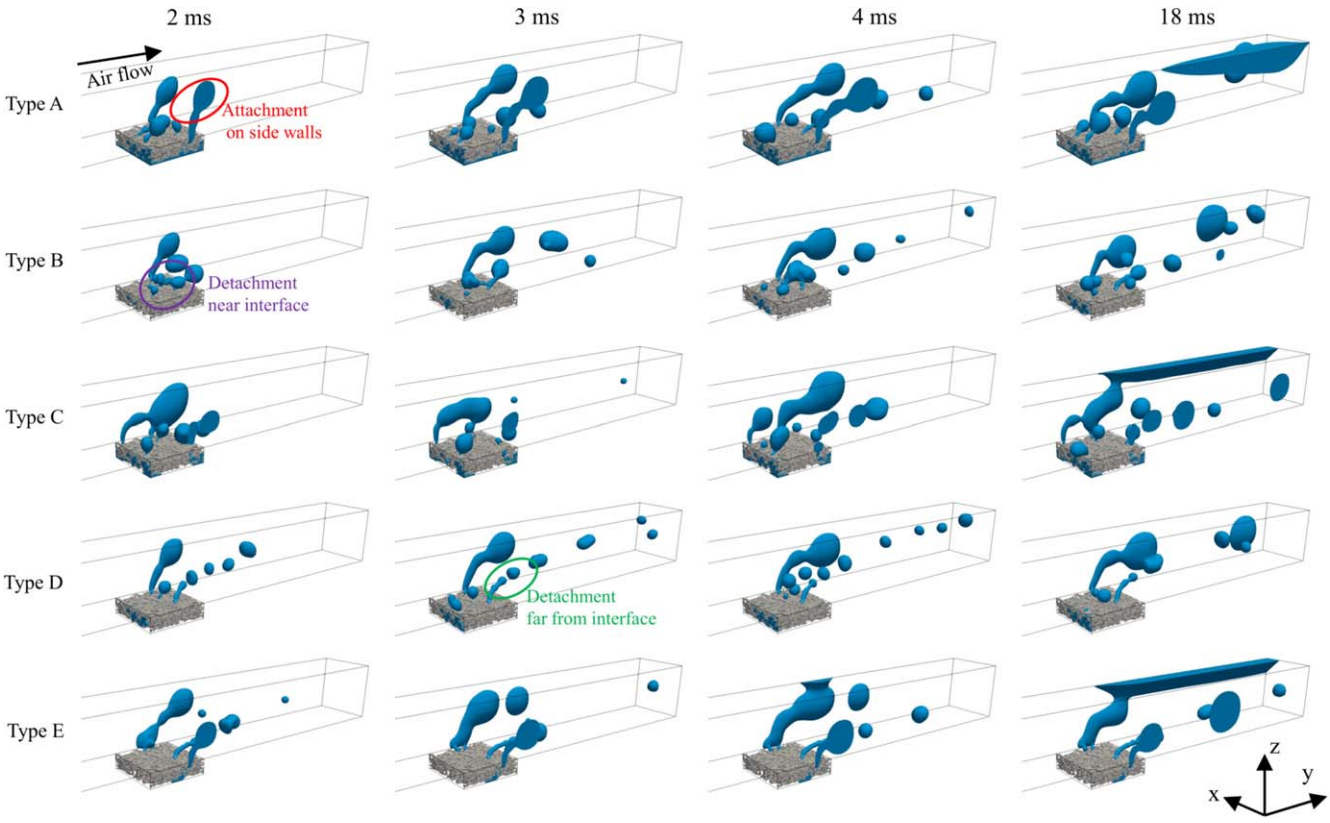

Figure 7. GC water distribution corresponding to Type A-E liquid injections at 2 ms, 3 ms, 4 ms, and 18 ms.

in water saturation. Liquid injections from Type B and Type D GDLs reduce water attachment on the sidewalls and facilitate rapid stabilization at lower water saturation levels. In contrast, higher water saturation in other scenarios is attributed to increased water attachment on the sidewalls. Comparative analysis of the GC distribution at 18 ms, as shown in Fig. 7, reveals that the differing water saturation levels between the GC connected to Type A and those connected to Type C and Type E GDLs are due to the connectivity of the water along the corners. A continuous flow at the GC corner remains stable once it is established, facilitating the water removal and also stabilization of the water amount. However, the discrete flow in the Type A GC moves slowly without continuous liquid inertial force from the newly breakthrough liquid. An initial decrease during GC water accumulation indicates the initial drainage moment, as shown in Fig. 8b. There is no water flowing out of Type A GC in 4 ms because the large droplets detach and move slowly. Besides, attached water on the GC side wall moves much more slowly and hardly contributes to the variations during GC water accumulation. In other GCs, the droplet removal from the GC central region without any attachment leads to variations in the GC water accumulation process.

GC pressure drop is also studied and the results are shown in Fig. 8c. All time-varying GC pressure drop values increase rapidly before initial drainage, followed by frequent fluctuation with varying magnitude. It can be found that Type B, Type D, and Type E GCs have an initial drainage before 4 ms in Fig. 8b. As a result, these three GCs show more rapid statistical stabilization of pressure drop. Besides, Type A and Type C GCs take a longer time to reach this state due to their slow initial drainage. It is hard to see a strong relationship between the GC pressure drop and water saturation level based on Figs. 8a, 8c. For example, Type B and Type D GCs have smaller liquid accumulation but a larger gas pressure drop; Conversely, Type E has relatively large liquid accumulation but a smaller gas pressure drop. However, the fluctuation level between pressure drop and water saturation seems to be related. Specifically, Type C and Type E GCs have smaller oscillations while the other three have stronger ones, especially the Type A GC. Observing their water flow type, it can be found that the movement of attached water along the GC is beneficial to reducing the pressure drop, which is related to the GC hydrophilic treatment. Small detached droplets contribute to the smaller fluctuation of pressure drop, which is related to the GDL pore structure near the liquid breakthrough locations. However, a lot of small droplets can merge into a large droplet before flowing out of GCs, thus the detachment frequency of droplets is also a potential factor related to the pressure drop. In addition, by comparing water distribution within Type A and Type E GCs in Fig. 7, small detached droplets close to the GDL/GC interface (GC bottom surface) have little effect on the pressure drop. The pressure drop increases as the drop grows larger and moves at a certain height above the interface (see Type A and Type B GC water flow at 18 ms in Fig. 7).

***Effect of electrode boundary conditions.*—**In previous interface-resolved two-phase flow simulations in both GDLs and channels, the motion of the gas flowing toward the catalyst layer is usually ignored. Regardless of whether this impacts the liquid flow, the reaction utilization (or stoichiometric number) will clearly be incorrect at the cell level. A full layer of liquid (in the GDL) effectively blocks gas transport to the MPL or catalyst layer and is physically unrealistic. In practice, if the flow is steady-contiguous, there must be two sets of percolating paths for both liquid and gas flows in opposite directions. In studies based on partial injection, the remaining portion of the GDL boundary is generally treated as an impermeable wall, thereby impeding oxygen from flowing out of the GDL. To facilitate simultaneous liquid-gas counter-flow in GDLs, one previous study proposed a novel idea[45] based on a modified boundary condition for the volume fraction α_l which is consistent with the so-called transferred-substance-state formulation,[77] for both single-phase and multi-phase chemically-reacting mass transfer problems, as found in catalytic converters, stirred tanks, and other

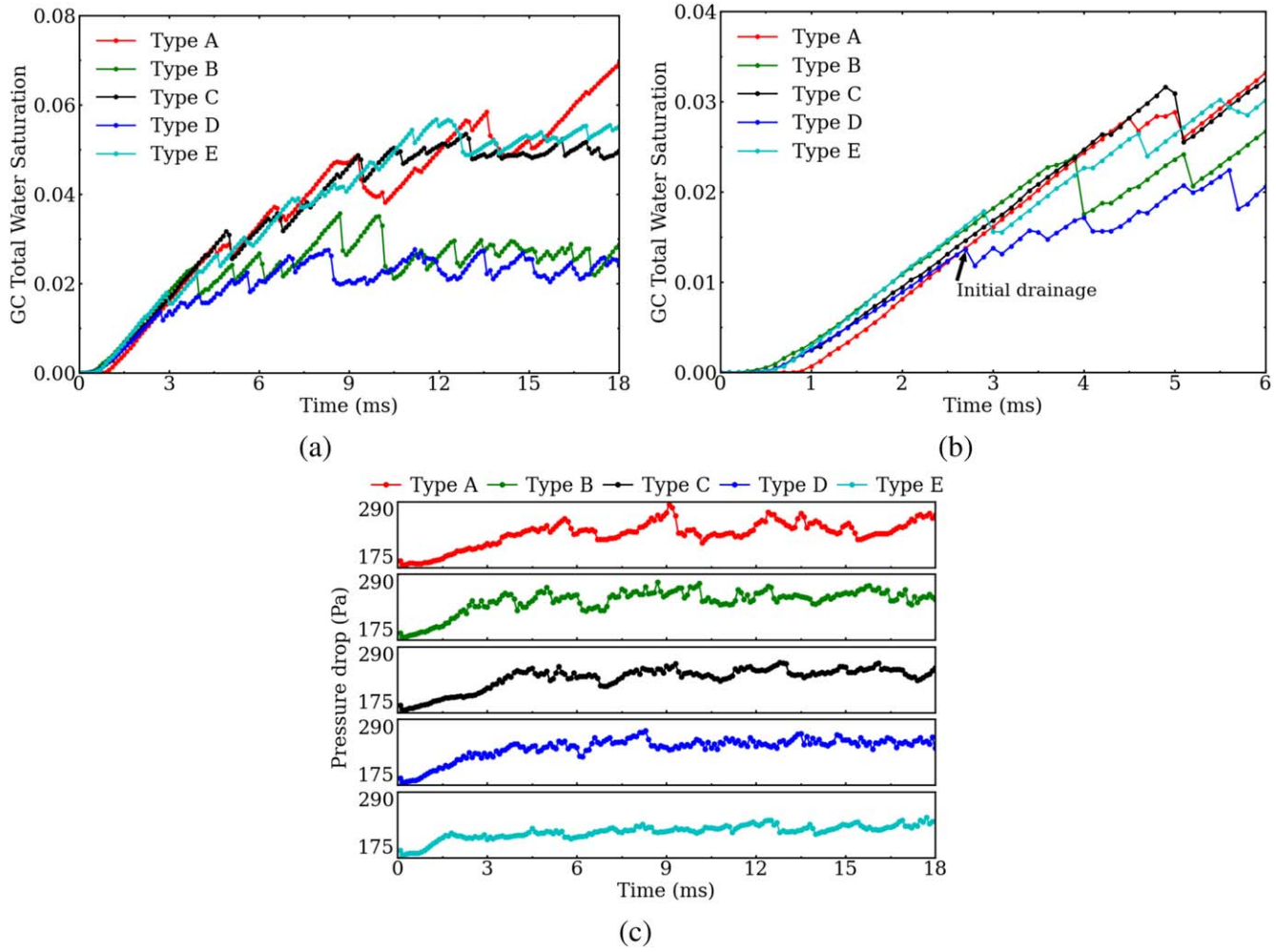

Figure 8. Time-dependent total water saturation and pressure drop within GC. (a) GC total water saturation. Calculation of GC total water saturation only considers the region where water may flow through, namely, the part above and after GDL along the airflow direction; (b) GC total water saturation before 6 ms; (c) Pressure drop.

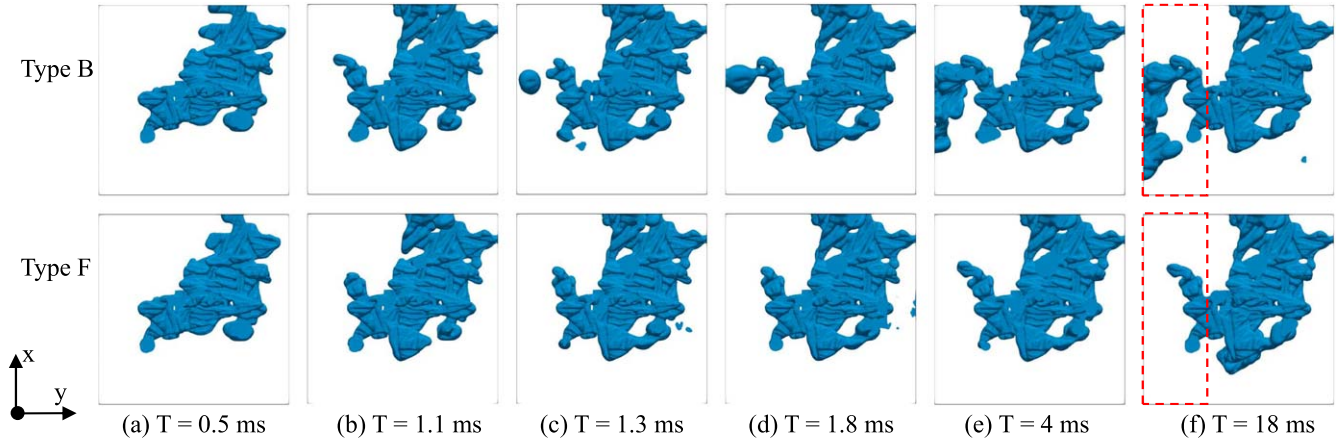

Figure 9. Top view (perpendicular to the x-y plane) of water distribution evolution in Type B and F GDLs.

applications. Such a technique would appear to be well-suited to Eulerian-Eulerian methods where the liquid-gas front is not resolved. Some discussion on the subject may be found in Beale et al.[78,79] However, there are still some outstanding numerical issues to be addressed; for example, with front-resolving schemes, depending on how the liquid-gas interface is constructed (algebraically or geometrically), essentially as a 3-D Dirac delta function, from the prescribed boundary values for $\alpha_l \neq 0, 1$ at the wall. Further research on the subject is in progress. It is noted that treating the problem as purely one in fluid dynamics means ignoring important within-phase and inter-phase phenomena due to associated combined mass and heat transfer. These will generally contribute to drop formation and evolution in gases (and bubbles in liquids) and need to be considered.

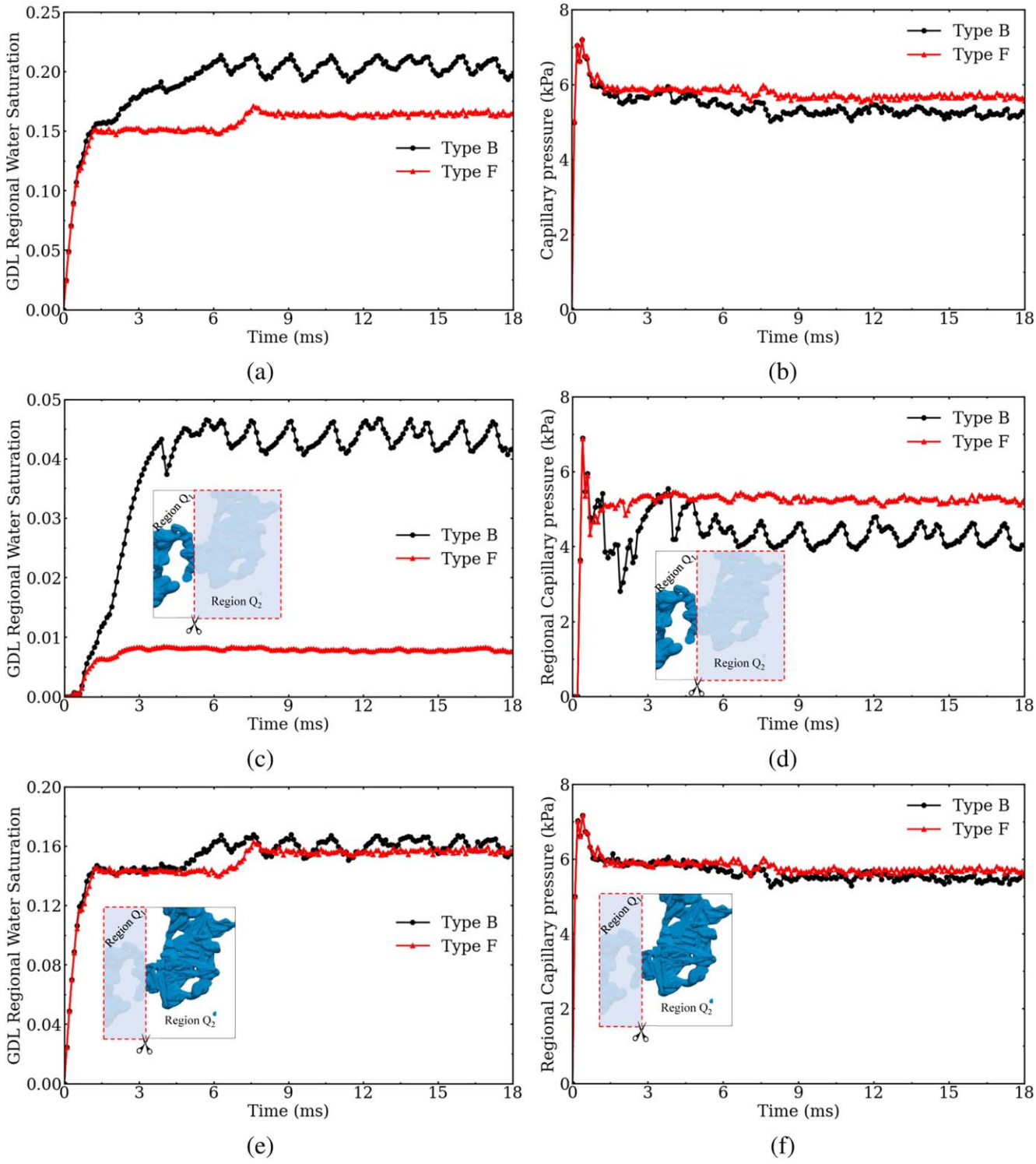

Figure 10. Comparison between Type B and F GDL time-varying total and regional water saturation level and capillary pressure.

Considering above issues related to the boundary and internal α_l values, in the present study, a stable boundary condition, $p = 0$, $\nabla\alpha_l = 0$, $\nabla\mathbf{U}\cdot\hat{\mathbf{n}} = 0$, is employed to the four corners (marked in yellow) of Type F GDL to observe the counter-flow dynamics of liquid and gas. However, it is worth mentioning that this boundary condition simplifies the physical reality due to the absence of gas species transport and electrochemical reactions. Gas species diffusion is not considered here but only multi-phase liquid-gas fluid mechanics (momentum not scalar transport). The selected boundary condition pertains more directly to fluid dynamic behaviors. The motivation is to propose a method to realize bidirectional liquid-gas flow on the liquid inlet surface of a GDL Section by utilizing the existing numerical boundary conditions and VOF method, and to study the fundamental dynamics of liquid-gas interaction with or without considering the outflow of the reactive gas from the GDL. Based on the current first-step investigation, future work is expected to incorporate more realistic GDL gas outlet boundary conditions that accurately reflect the coupled processes of species transport, electrochemical reactions, and thermal effects. Such enhancements will facilitate a more comprehensive representation of the operational conditions within

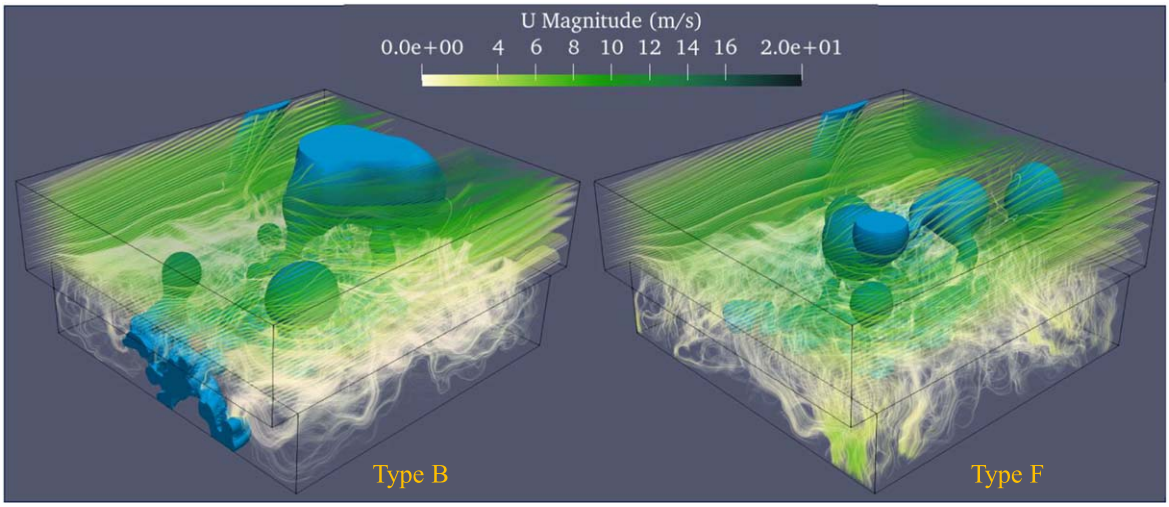

Figure 11. Liquid phase distribution (Blue color) and gas phase velocity streamlines (color bar) within GDL and GC of Type B and Type F at T = 4 ms.

fuel cells and are expected to provide deeper insights into the complex liquid-gas interactions between these various physical processes within the GDL. In reality, positions for liquid inlet and positions for air outlet would move with time.

Figure 9 presents a top view of the water distribution in the Type B and Type F GDLs. Initially, at T = 0.5 ms, both GDLs display comparable water behaviors. However, a significant divergence in water distribution is observed by T = 1.3 ms within the region encircled in red in Fig. 9(e). Specifically, the GDL of Type B exhibits phenomena such as droplet breaking and reconnection, followed by progressively wider spreading over time. It is speculated such a difference is due to the fact that the air outflow in Type F GDL may hinder the water spreading behavior after the breakthrough in Type B GDL.

Figures 10a–10b compare the time-varying GDL total water saturation and capillary pressure in Type B and Type F GDLs. Initially, both scenarios show similar patterns of time-dependent increase in water saturation and capillary pressure until 1 ms. Subsequently, the water saturation in Type F GDL becomes statistically stable, settling at a lower level compared to that observed in Type B. In contrast, the capillary pressure in Type F stabilizes at a slightly higher value. Notably, Type F GDL does not display the large quasi-periodic oscillations in water saturation nor the irregular fluctuations in capillary pressure observed in Type B. Instead, these phenomena are supplanted by much smaller fluctuations in both parameters. Regional water behavior in two subregions, e.g., Region Q_1 and Region Q_2, are further analyzed in Figs. 10c–10f. Note that the regional water saturation is calculated based on the ratio of regional water volume to the total GDL pore volume. Calculation of regional capillary pressure only uses the pressure information in each region because it is based on the area-weighted average.

It is found that the main difference caused by the liquid-gas inlet and outlet boundary treatment of the two GDLs is located in the region Q_1, as shown in Figs. 10c–10d. Type B GDL shows a much higher regional water saturation and lower capillary pressure in this region compared with the Type F scenario, accompanied by strong quasi-periodic oscillations in the latter duration due to minor water advancing and receding behavior within the GDL. The regional water saturation and capillary pressure magnitude of two GDLs in Figs. 10e–10f are close, though the oscillations in the Type B case still exist. Consequently, it is thought that the presence of GDL air outflow is associated with increasing capillary pressure within Region Q_1, which stops the penetration of liquid water through the pores in this region and avoids generating heavy water spreading behavior. Furthermore, the rapid decrease of regional capillary pressure during 1-2 ms does not cause fluctuation of the relevant water saturation. This may result from the included iso-surface of breaking droplets during the calculation of capillary pressure, for the small average capillary pressure of an isolated droplet will further decrease the average capillary pressure in Region Q_1. With the reconnection of liquid in this area, the high capillary pressure in the main liquid will transfer to the whole Region Q_1 again, which leads to the rapid increase of capillary pressure after 2 ms. Excluding the breaking droplets in the calculation of capillary pressure might be another option no matter using the surface pressure or curvature information. Besides, in Figs. 10a–10b, 10e–10f, an increase in water saturation and a slight decline in capillary pressure are observed in both GDLs between 4 ms and 8 ms. This increased water saturation is found to occur in Region Q_2 by filling empty pores, as shown in Fig. B·1. However, Type F GDL exhibits a wider filling area and delayed filling time, which may caused by the presence of air outflow boundary conditions. To obtain more detail, a further investigation is followed by considering the airflow behavior.

Figure 11 exhibits the gas phase velocity streamline and liquid phase distribution inside GC and GDL of Type B and Type F at T = 4 ms. By altering only the boundary condition at GDL bottom four corners with or without air outflow, gas and liquid phases show different water transport in the two scenarios. It is found that in Type B, the gas velocity streamlines terminate or change direction near the GDL bottom because of the wall boundary condition, while Type F exhibits closely spaced gas velocity streamlines converging toward the four bottom corners of the GDL, together with a larger velocity. As a result, the gas velocity streamlines in Type B appear more random and chaotic. Liquid distribution within both the GDL and GC are greatly different. Apart from the distinct GDL water accumulation discussed in the former parts, water behavior in GCs differs, e.g., different droplet breakthrough and detachment behavior in time and space. Once liquid appears in the GC, the airflow forces the liquid water to detach and move. Simultaneously, the gas phase is forced to change the flow pathways above the GDL/GC interface. Some airflow can be accelerated or obstructed into the GDL. Due to the different treatments at the GDL bottom, the airflow difference within GDLs gets increasingly different. According to different boundary condition treatments, the effect of two-phase interactions on two-phase behavior has been observed. However, the complex two-way coupling two-phase interaction mechanisms are still unclear, including determining the dominant phase (liquid or gas) and dominant region (GC or GDL) during interactions. More studies need to be conducted in future work to address these gaps.

Conclusions

Liquid-gas two-phase counter-flow within a fibrous GDL and GC assembly is investigated by utilizing the volume of fluid method. The

impact of GDL liquid water inlet size, shape, and location has been explored under a constant liquid mass flow rate. Furthermore, the two-phase flow with/without considering the GDL gas outlet is compared.

The water saturation and capillary pressure of all investigated GDLs with full/partial water injection reach statistical stabilization in the range of 15%–25% and 5–6 kPa, respectively, accompanied by varying degrees of oscillation. A full-area liquid injection (Type A) leads to the lowest capillary pressure, the highest water saturation within the GDL and GC, and the largest fluctuating magnitude of GC pressure drop. The invading liquid is more likely to find pathways formed by the large pores prior to breakthrough, avoiding the increase in capillary pressure caused by small pores near the partial liquid injection. Plenty of the invading water in Type A GDL stops rising near the liquid inlet, contributing to the highest water saturation. Thus, the full liquid injection should be guaranteed to occur less in real applications, as the extensive water accumulation near the liquid inlet impedes the transport of reactant gases to the catalyst layer. Water saturation near the injection rapidly reaches a relatively stable state, while the middle region, between relative thicknesses 0.2 and 0.6, owns a slower stabilization. Among partial liquid injection scenarios, a quasi-periodic variation of water saturation after breakthrough is found, which relates to the phenomenon of water advancing and receding behavior within the porous GDL. Besides, the liquid inlet location shows a higher impact than the inlet size. Partial liquid injection resulted in faster GDL breakthrough and faster initial discharge in the GC due to increased liquid inlet velocity. Besides, there is no strong correlation between GC water saturation and gas pressure drop. The GC pressure drop fluctuates in a certain range at different degrees in all scenarios, whereas only the GCs associated with partial liquid injection reach a statistical stabilization of GC water saturation. The relatively stable saturation level is mostly related to the droplet breakthrough and detachment position, which is further affected by partial liquid injection locations. Enhancing water attachment on side walls and decreasing detached droplet size near the GDL/GC interface helps reduce the gas pressure drop and stabilize the GDL water saturation.

A different two-phase flow behavior can be observed when the widely-neglected air outflow at the GDL/electrode interface is considered, e.g., a two-phase counter-flow situation. Compared with the situation with merely a liquid inlet, the presence of air outflow results in lower water saturations with less fluctuations, but slightly higher capillary pressures, because it eliminates the spreading and accumulation of liquid flowing through the smaller pores. Without GDL air outflow, the gas velocity streamlines terminate and turn in a direction near the GDL bottom, showing a high sensitivity to GC liquid variation. However, in the comparative case, the streamlines are more stable and are directed toward the air outflow boundary. The increase in water saturation after the initial breakthrough comes from filling pores in different regions in these two scenarios. Following the different water dynamics caused by including the GDL air outflow, an increased difference in GC water behavior is observed compared to the base case. There is found to be some new liquid-gas interaction when involving the GDL air outlet boundary condition. However, it is hard to conduct force analysis to obtain their interaction mechanism, which is expected to be realized in future work.

This study aims to introduce air outlets at the GDL/electrode interface by combining geometric design and existing boundary conditions. An even more realistic air outlet boundary condition for a two-phase counter-flow interface capturing method still needs in-depth exploration from the numerical perspective to develop the current interface capturing method and advanced boundary conditions. In addition, incorporating multi-phase species transport conservation, multi-species formulations, phase change, and gas solution will account for a varying composition of air gas in fuel cells.

Acknowledgments

D. Yang would like to acknowledge the Chinese Scholarship Council (grant number: 202006070174). The authors thank Dr. Eugen Hoppe for constructing a stereolithography file of the porous material used in this study. Early discussions with Dr. Norbert Weber, Dr. Holger Marschall, and Prof. Werner Lehnert on matters related to the subject of this paper were appreciated by the authors. Calculations were performed on the high-performance computing cluster of National Academic Infrastructure for Supercomputing in Sweden (NAISS) with project number 2018-05973.

Appendix A. Comparison Calculation Methods for P_c

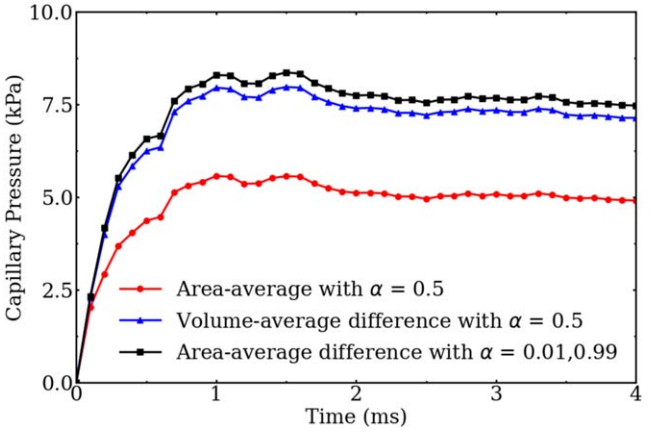

Figure A·1. Comparison of three existing capillary pressure calculations using the GDL with a full liquid inlet (Type A). "Area-average with $\alpha = 0.5$" refers to the method of employing the area-weighted average pressure on the iso-surface where $\alpha = 0.5$.[20] "Volume-average difference with $\alpha = 0.5$" is determined by the difference in volume-weighted average pressure between the volumes with $\alpha \geq 0.5$ and $\alpha < 0.5$.[64] "Area-average difference with $\alpha = 0.01$ and $\alpha = 0.99$" is derived by mapping the pressure at the iso-surfaces $\alpha = 0.99$ and $\alpha = 0.01$ onto an iso-surface at $\alpha = 0.5$, and subsequently calculating their area-weighted average values based on the same surface area at $\alpha = 0.5$.[68]

Appendix B. Increased Water Saturation in Type B and Type F GDLs

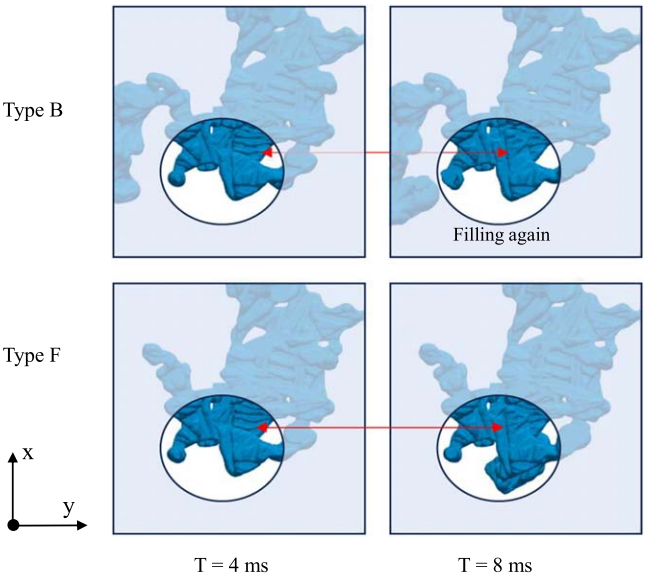

Figure B·1. Water saturation increases between 4 ms and 8 ms by filling empty pores in Type B and Type F GDLs.

ORCID

Danan Yang https://orcid.org/0000-0001-9314-1205
Steven B. Beale https://orcid.org/0000-0002-6755-9111
Himani Garg https://orcid.org/0000-0002-5223-0567
Martin Andersson https://orcid.org/0000-0001-5057-4908

References

1. A. Ozden, S. Shahgaldi, X. Li, and F. Hamdullahpur, *Progress in Energy and Combustion Science*, **74**, 50 (2019).
2. P. C. Okonkwo and C. Otor, *International Journal of Energy Research*, **45**, 3780 (2021).
3. Q. Chen, Z. Niu, H. Li, K. Jiao, and Y. Wang, *International Journal of Hydrogen Energy*, **46**, 8640 (2021).
4. M. Siegwart, R. P. Harti, V. Manzi-Orezzoli, J. Valsecchi, M. Strobl, C. Grünzweig, T. Schmidt, and P. Boillat, *J. Electrochem. Soc.*, **166**, F149 (2019).
5. V. Manzi-Orezzoli, M. Siegwart, M. Cochet, T. J. Schmidt, and P. Boillat, *J. Electrochem. Soc.*, **167**, 054503 (2019).
6. S. Chevalier et al., *J. Electrochem. Soc.*, **164**, F107 (2016).
7. A. Mularczyk, Q. Lin, M. J. Blunt, A. Lamibrac, F. Marone, T. J. Schmidt, F. N. Büchi, and J. Eller, *J. Electrochem. Soc.*, **167**, 084506 (2020).
8. R. B. Ferreira, D. Falcão, V. Oliveira, and A. Pinto, *Journal of Power Sources*, **277**, 329 (2015).
9. Z. Lu, M. M. Daino, C. Rath, and S. G. Kandlikar, *International Journal of Hydrogen Energy*, **35**, 4222 (2010).
10. C. Hirt and B. Nichols, *J. Comput. Phys.*, **39**, 201 (1981).
11. F. H. Harlow and A. A. Amsden, *J. Comput. Phys.*, **8**, 197 (1971).
12. C. T. Crowe, M. P. Sharma, and D. E. Stock, *Journal of Fluids Engineering*, **99**, 325 (1977).
13. C. Wang and P. Cheng, *International Journal of Heat and Mass Transfer*, **39**, 3607 (1996).
14. C. Wang and P. Cheng, *Advances in Heat Transfer*, **30**, 93 (1997).
15. M. Andersson, A. Mularczyk, A. Lamibrac, S. Beale, J. Eller, W. Lehnert, and F. Büchi, *Journal of Power Sources*, **404**, 159 (2018).
16. J. Liao, G. Yang, Q. Shen, S. Li, Z. Jiang, H. Wang, G. Zhang, Z. Li, and B. Sun, *Transport in Porous Media*, **148**, 335 (2023).
17. K. G. Lyras, B. Hanson, M. Fairweather, and P. J. Heggs, *J. Comput. Phys.*, **407**, 109224 (2020).
18. Y. Sun, C. Bao, Z. Jiang, X. Zhang, and T. Gao, *Journal of Power Sources*, **448**, 227352 (2020).
19. Z. Y. Ahmad, S. Didari, J. Moon, and T. A. Harris, *ECS Trans.*, **45**, 89 (2013).
20. D. Niblett, A. Mularczyk, V. Niasar, J. Eller, and S. Holmes, *Journal of Power Sources*, **471**, 228427 (2020).
21. Y. Liu, C. Tang, M. Kohrn, B. Shi, Z. Wang, M. Wick, S. Pischinger, and J. Andert, *Journal of Power Sources*, **529**, 231221 (2022).
22. L. Zhang, S. Liu, Z. Wang, and R. Li, *Journal of Power Sources*, **554**, 232276 (2023).
23. Z. Niu, Z. Bao, J. Wu, Y. Wang, and K. Jiao, *Applied Energy*, **232**, 443 (2018).
24. Z. Niu, J. Wu, Z. Bao, Y. Wang, Y. Yin, and K. Jiao, *International Journal of Heat and Mass Transfer*, **139**, 58 (2019).
25. X. Zhou, Z. Niu, Z. Bao, J. Wang, Z. Liu, Y. Yin, Q. Du, and K. Jiao, *Journal of Power Sources*, **437**, 226933 (2019).
26. D. Jiao, K. Jiao, Z. Niu, S. Zhong, and Q. Du, *International Journal of Energy Research*, **44**, 4438 (2020).
27. S.-H. Lee, J. H. Nam, C.-J. Kim, and H. M. Kim, *International Journal of Hydrogen Energy*, **46**, 33957 (2021).
28. S. Zhou, G. Xie, H. Hu, and M. Ni, *International Journal of Hydrogen Energy*, **48**, 10644 (2023).
29. D. Yang, H. Garg, and M. Andersson, *International Journal of Hydrogen Energy*, **48**, 15677 (2023).
30. G. Dong, G. Huang, Z. Wu, Z. Li, P. Ming, and L. Zhang, *International Journal of Hydrogen Energy*, **50**, 18 (2024).
31. Z. Niu, Y. Wang, K. Jiao, and J. Wu, *J. Electrochem. Soc.*, **165**, F613 (2018).
32. A. Z. Weber et al., *J. Electrochem. Soc.*, **161**, F1254 (2014).
33. A. D. Santamaria, P. K. Das, J. C. MacDonald, and A. Z. Weber, *J. Electrochem. Soc.*, **161**, F1184 (2014).
34. K. N. Kim, J. H. Kang, S. G. Lee, J. H. Nam, and C.-J. Kim, *Journal of Power Sources*, **278**, 703 (2015).
35. Y. Ira, Y. Bakhshan, and J. Khorshidimalahmadi, *International Journal of Hydrogen Energy*, **46**, 17397 (2021).
36. L. Guo, L. Chen, R. Zhang, M. Peng, and W.-Q. Tao, *Energy*, **253**, 124101 (2022).
37. D. Niblett, V. Niasar, S. Holmes, A. Mularczyk, J. Eller, R. Prosser, and M. Mamlouk, *Journal of Power Sources*, **555**, 232383 (2023).
38. X. Shi, D. Jiao, Z. Bao, K. Jiao, W. Chen, and Z. Liu, *International Journal of Hydrogen Energy*, **47**, 6247 (2022).
39. R. Lin, M. Dong, S. Lan, and M. Lou, *Energy*, **262**, 125372 (2023).
40. S. Zhang, S. Beale, W. Lehnert, and W. Schröder, *Lehr-und Forschungsgebiet Modellierung in der elektrochemischen Verfahrenstechnik (FZ Jülich)* (2020).
41. Y. Yu, S. Chen, and H. Wei, *International Journal of Heat and Mass Transfer*, **212**, 124275 (2023).
42. A. Bazylak, D. Sinton, Z.-S. Liu, and N. Djilali, *Journal of Power Sources*, **163**, 784 (2007).
43. D. H. Jeon, *Journal of Power Sources*, **475**, 228578 (2020).
44. Z. Niu, K. Jiao, Y. Wang, Q. Du, and Y. Yin, *International Journal of Energy Research*, **42**, 802 (2018).
45. S. B. Beale, M. Andersson, N. Weber, H. Marschall, and W. Lehnert, *ECS Trans.*, **98**, 305 (2020).
46. C. Dopazo, *J. Fluid Mech.*, **81**, 433 (1977).
47. V.-T. Nguyen and W.-G. Park, *Computers & Fluids*, **152**, 104 (2017).
48. J. Brackbill, D. Kothe, and C. Zemach, *J. Comput. Phys.*, **100**, 335 (1992).
49. J. P. Boris and D. L. Book, *J. Comput. Phys.*, **11**, 38 (1973).
50. S. T. Zalesak, *J. Comput. Phys.*, **31**, 335 (1979).
51. M. Rudman, *International Journal for Numerical Methods in Fluids*, **24**, 671 (1997).
52. O. Ubbink and R. Issa, *J. Comput. Phys.*, **153**, 26 (1999).
53. S. Muzaferija, *Nonlinear Water-wave Interaction* (WIT Press, Southampton, UK) 59–100 (1999).
54. T. Marić, D. B. Kothe, and D. Bothe, *J. Comput. Phys.*, **420**, 109695 (2020).
55. P. Personnettaz, P. Beckstein, S. Landgraf, T. Köllner, M. Nimtz, N. Weber, and T. Weier, *Journal of Power Sources*, **401**, 362 (2018).
56. Z. Jiang, G. Yang, Q. Shen, S. Li, J. Liao, X. Yang, and J. Sun, *Materials Today Communications*, **37**, 107633 (2023).
57. R. Lin, S. Lan, X. Wu, and Z. Hao, *Renewable Energy*, **222**, 119900 (2024).
58. J. Sim, M. Kang, and K. Min, *Journal of Power Sources*, **544**, 231912 (2022).
59. D. Yang, H. Garg, and M. Andersson, *International Journal of Hydrogen Energy*, **85**, 635 (2024).
60. M. Andersson, S. Beale, U. Reimer, W. Lehnert, and D. Stolten, *International Journal of Hydrogen Energy*, **43**, 2961 (2018).
61. L. Gamet, M. Scala, J. Roenby, H. Scheufler, and J.-L. Pierson, *Computers & Fluids*, **213**, 104722 (2020).
62. J. López, A. Esteban, J. Hernández, P. Gómez, R. Zamora, C. Zanzi, and F. Faura, *J. Comput. Phys.*, **444**, 110579 (2021).
63. S. Sakaida, Y. Tabe, K. Tanaka, and M. Konno, *International Journal of Hydrogen Energy*, **46**, 7464 (2021).
64. A. Mularczyk, Q. Lin, D. Niblett, A. Vasile, M. J. Blunt, V. Niasar, F. Marone, T. J. Schmidt, F. N. Buhi, and J. Eller, *ACS Applied Materials & Interfaces*, **13**, 34003 (2021).
65. N. K. Palakurthi, S. Konangi, A. Kishore, K. Comer, and U. Ghia, *European Journal of Mechanics-B/Fluids*, **67**, 357 (2018).
66. J. D. Fairweather, P. Cheung, J. St-Pierre, and D. T. Schwartz, *Electrochemistry Communications*, **9**, 2340 (2007).
67. H. S. Rabbani, V. Joekar-Niasar, and N. Shokri, *J. Colloid Interface Sci.*, **473**, 34 (2016).
68. S. Konangi, N. K. Palakurthi, N. K. Karadimitriou, K. Comer, and U. Ghia, *Advances in Water Resources*, **147**, 103792 (2021).
69. L. Zhang, S. Liu, Z. Wang, R. Li, and Q. Zhang, *International Journal of Hydrogen Energy*, **47**, 17713 (2022).
70. N. Zamel, X. Li, J. Becker, and A. Wiegmann, *International Journal of Hydrogen Energy*, **36**, 5466 (2011).
71. F. Bresciani, A. Casalegno, G. Varisco, and R. Marchesi, *International Journal of Energy Research*, **38**, 602 (2014).
72. R. Lenormand, E. Touboul, and C. Zarcone, *J. Fluid Mech.*, **189**, 165 (1988).
73. S. Wang, S. Guan, L. Zhang, F. Zhou, J. Tan, and M. Pan, *Journal of Power Sources*, **533**, 231402 (2022).
74. M. A. Hickner and K. S. Chen, *International Conference on Fuel Cell Science, Engineering and Technology***37645**, 65 (2005).
75. Y. Ding, H. Bi, and D. Wilkinson, *Journal of Power Sources*, **195**, 7278 (2010).
76. Y. Ding, H. Bi, and D. Wilkinson, *Journal of Power Sources*, **196**, 6284 (2011).
77. D. Spalding, *International Journal of Heat and Mass Transfer*, **1**, 192 (1960).
78. S. B. Beale, S. Zhang, M. Andersson, R. T. Nishida, J. G. Pharoah, and W. Lehnert, *Heat and Mass Transfer in Fuel Cells and Stacks* (Springer Singapore)485 (2020).
79. S. B. Beale, D. H. Schwarz, M. R. Malin, and D. B. Spalding, *Computational Thermal Sciences: An International Journal*, **1** (2009).